Assimilation of Himawari-8 Imager Radiance Data with the WRF-3DVAR system for the prediction of Typhoon Soudelor

Feifei Shen[1,2,3*],Aiqing Shu[1],Hong Li [4],Dongmei Xu[1,2,3],Jinzhong Min[1]

1. The Key Laboratory of Meteorological Disaster, Ministry of Education (KLME)/Joint International Research Laboratory of Climate and Environment Change (ILCEC)/Collaborative Innovation Center on Forecast and Evaluation of Meteorological Disasters (CIC-FEMD), Nanjing University of Information Science & Technology, Nanjing 210044, China

2.   Heavy Rain and Drought-Flood Disasters in Plateau and Basin Key Laboratory of Sichuan Province, Chengdu, China

3.   The Institute of Atmospheric Environment, China Meteorological Administration, Shenyang 110000, China

4.   Shanghai Typhoon Institute,China Meteorological Administration,Shanghai 200030, China

Abstract

20   Himawari-8 is a new generation geostationary meteorological satellite launched

21 by Japan Meteorological Agency. It carries the Advanced Himawari Imager (AHI)

22 onboard, which can continuously monitor high-impact weather events with high

23 frequency space and time. The assimilation of AHI radiance data was implemented

24 with the three-dimensional variational data assimilation system of Weather Research

25 and Forecasting model for the analysis and prediction of Typhoon Soudelor (2015) in

26 the Pacific Typhoon season. The effective assimilation of AHI radiance data in

27 improving the forecast of the tropical cyclone during its rapid intensification has been

28 realized. The results show that after assimilating the AHI radiance data under clear

29 sky conditions, the typhoon position in the background field of the model was

30 effectively corrected compared with the control experiment without AHI radiance data

31 assimilation. It is found that the assimilation of AHI radiance data is able to improve

32 the analyses of the water vapor and wind in typhoon inner-core region. The analyses

33 and forecasts of the minimum sea level pressure, the maximum surface wind, and the

34 track of the typhoon are further improved.

35   **Key words:** Weather Research and Forecasting model; Three-Dimensional

36 Variational Data Assimilation; AHI Radiance Data; Typhoon

1. Introduction

In recent years, although researchers have made great progress in the field of numerical weather prediction (NWP), the huge challenges are encountered in the accurate forecasts of tropical cyclones (TCs) with rapid intensifications (DeMaria et al., 2014). The predictability of these TCs is limited because it entails complex multi-scale dynamic interactions (Minamide and Zhang 2018). These interactions include environmental airflows, TC vortex interactions, atmosphere-ocean interactions, and the effects of mesoscale and micro-convective scale, together with the microphysics and atmospheric radiation. In order to attain a better initial condition and improve the accuracy of the forecast, data assimilation seeks to fully utilize the observations. The life span of most TCs is over the ocean where conventional observations are relatively insufficient compared to the land. Therefore, by analyzing observed data from satellites and planes over the ocean, it is crucial to adopt effective data assimilation (DA) methods to improve the analysis and forecast of TCs.

With the rapid development of atmospheric radiative transfer model, many numerical weather prediction centers have adopted variational DA method to assimilate a variety of radiance data from different satellite observation instruments (Bauer et al., 2011; Buehner et al., 2016; Derber et al., 1998; Hilton et al., 2009; Kazumori et al., 2014; McNally et al., 2006; Prunet et al., 2000). These data can take up 90% of all data used in global DA system and can improve the accuracy of the numerical model results strikingly (Bauer et al., 2010). Some researches demonstrated

59 that in global model, satellite radiance DA makes more contribution to improving the

60 accuracy of the numerical model results than conventional observation DA does

61 (Zapotocny et al., 2007, Yan et al., 2010; Geer et al., 2017).

62 Generally speaking, radiance data are derived from microwave and infrared

63 detecting instruments, which are from polar-orbit satellites and geostationary satellites,

64 respectively. Polar-orbit satellites cover the sphere of all the earth, thereby suitable for

65 global NWP models (Jung et al., 2008). Besides, they have finer resolutions compared

66 to geostationary satellites (Li et al., 2017; Shen et al., 2015; Xu et al., 2013). However,

67 it is highlighted that they are not able to generate continuous observations for a fixed

68 regional area and so may miss rapidly intensified TCs or storms. On the contrary,

69 because geostationary satellites rotate with the earth, although their resolutions are

70 lower than that of polar-orbit satellites, they can capture the formation and

71 development of mesoscale convective systems by continuous monitoring (Montmerle

72 et al., 2007; Stengel et al., 2009; Zou et al.,2011).

73 Geostationary satellites are able to continuously detect a region at a higher

74 frequency, thus observing TCs over the vast ocean effectively. As the first new

75 generational geostationary satellite, Himawari-8 plays a pioneering role for the

76 geosynchronous imagers to be launched in US, China, Korea and Europe. It has an

77 advanced imager called Advanced Himawari Imager (AHI) with 16 visible and

78 infrared bands, including 3 moisture channels, which can conduct a full-disk scan

79 every 10 minutes. Meanwhile, it can also acquire regional scanning images and that is

to say it can scan the Japan and the target areas every 2.5 minutes. Compared to the early geosynchronous imagers, AHI has more spectrum bands and this can monitor the state of atmosphere with a higher frequency.

In recent years, some experts and scholars have carried out some studies on the data assimilation of geostationary satellite observations. Firstly utilizing Gridpoint Statistical Interpolation (GSI) from National Centers for Environmental Prediction (NCEP), Zou, et al (2011) conducted direct assimilation on imagers' data from GOES-11 and GOES-12 to estimate their potential influences on quantitative precipitation forecasts (QPF) of coastal regions in the eastern part of American. They found that assimilating radiance data from GOES's imager has a remarkable improvement on 6 to 12 hour's QPF near northern Mexico Gulf coast. Their work was continued by Qin, et al (2013), which put thinned radiance data into GSI system to make a comprehensive investigation on the issue on combined assimilation of GOES Imager data together with Advance Microwave Sounding Unit-A (AMSU-A), Advance Microwave Sounding Unit-B (AMSU-B), Atmospheric Infrared Sounder (AIRS), Microwave Humidity Sounder (MHS), High Resolution Infrared Radiation Sounder (HIRS), GOES Sounder (GSN). The results showed the effect of single assimilation of AHI radiance data are better than combined assimilation in term of precipitation forecast. Zou, et al (2015) adopted the GSI system to assimilate radiance data from four infrared channels on GOES-13/15 and set up two experiments for comparison. A symmetric vortex was used for initialization in the first experiment and

an asymmetric counterpart for the other experiment. Results showed that direct

assimilation of GOES-13/15's radiance data could yield positive effects on the track

and intensity forecasts of hurricane "Debbie". As the new instrument of himawari-8,

there are few studies on the DA of himawari-8 data. Ma, et al (2017) used

four-dimensional ensemble variational (4DEnVar) DA in NCEP's GSI system to

assimilate radiance of three moisture channels of AHI radiance data under clear-sky

condition and then NCEP Global Forecast System (GFS) was utilized to estimate the

impacts of AHI radiance data assimilation on weather forecast. They found it had a

positive impact on the forecast of global vapor at high level of troposphere. Wang, et

al (2018) investigated the impact of assimilating three water vapor channels under

clear sky on the analysis and forecast of a rainstorm in Northern China with the

3DVAR method. It pointed out that the assimilation of AHI radiance data could

improve the wind and vapor fields and the accuracy of rainfall forecast in the first 6

hours lead time.

Although previous researches have made several achievements in satellite data

assimilation and application, it is still a challenge to make more effective use of the

new generational geostationary satellite imager data with high spatial and temporal

resolution. In most of the previous studies, researches usually use a 6 hour's or even

longer time interval with a coarse spatial resolution. Therefore, the rapid updating

assimilation techniques of the geostationary satellite radiance data have not been well

carried out at convective scale. This study intends to build a data assimilation system

aiming at AHI radiance data based on the new generational mesoscale Weather

Research and Forecasting (WRF) model. A case of Typhoon Soudelor is studied by

performing numerical simulation to address the impacts of convective DA on the

improvement of the initial conditions of TC and the enhancement of track and

intensity forecasts. Our study focuses mainly on assimilating the three water vapor

channels (6.2, 6.9, and 7.3μm) since they are very sensitive to the humidity in the

middle and upper troposphere and have a certain effect on the lower troposphere.

Thus, a large amount of effective atmospheric information can be provided for AHI

radiance data assimilation in the troposphere. The weighting functions for the three

channels are provided in Fig. 1.

Section 2 describes the observations and the data assimilation system. Introductions

to the typhoon case and the experimental setup are provided in section 3. The detailed

results in terms of the analyses and the forecasts are illustrated in section 4 before

conclusions are summarized in section 5.

2. Observational data and DA system

2.1 An introduction to Himawari-8 AHI radiance data

Himawari-8 satellite was launched by JMA to a geosynchronous orbit on 17

October 2014 and has begun its operational use since 7 July 2015 (Bessho et al.,

2016). It is located between the equator and 140.7°E, thus the earth is observed

between 60°N and 60°S meridionally and between 80°E and 160°W zonally.

Compared to its previous generation Himawari-7, its detective ability can get

143 significantly improved since the instrument AHI on Himawari-8. Besides, its device is

144 comparable to imagers on American GOES-R satellite (Goodman et al., 2012; Schmit

145 et al., 2005; Schmit et al., 2008; Schmit et al., 2017). AHI is able to provide a full-disk

146 image every 10 minutes and complete a scan over Japan every 2.5 minutes. AHI

147 conducts continuous scan and detection on a moving targeted typhoon. It has 16

148 channels covering visible, near-infrared, and infrared spectral bands with a resolution

149 of 0.5 km or 1 km, and 2 km respectively. Channel 8 to 10 (6.2, 6.9, and 7.3 μm) are

150 water vapor bands that are sensitive to the humidity in the middle and upper

151 troposphere (Di et al., 2016). Other channels (channel 11, 12, 16: 8.6 μm, 9.6 μm, and

152 13.3μm) are either monitoring other fields such as the thin ice clouds, volcanic SO_2

153 gas, the ozone or CO_2, or the atmospheric window channels (13-15: 10.4, 11.2, and

154 12.4 μm) function as monitors for ice crystal/water, low water vapor, volcanic ash, sea

155 surface temperature and other phenomena (Bessho et al., 2016).

156 *2.2 WRFDA system and AHI radiance data*

157 WRFDA system is designed by National Center for Atmospheric Research

158 (NCAR) and it contains 3DVAR, 4DVAR, Hybrid parts. This research is based on the

159 3DVAR method. An interface that is suitable for AHI DA is built in WRFDA system.

160 Currently, WRFDA is able to assimilate many conventional and unconventional

161 observations. In terms of satellite radiance data, this system is compatible with the

162 Radiative Transfer model of the Television and Infrared Observational Satellite

163 Operational Vertical sounder (RTTOV) and Community Radiative Transfer Model

164 (CRTM, Liu and Weng, 2006) as observation operators. In this study, CRTM is

165 utilized as the observation operator to simulate and compute AHI radiance data.

166 Estimating the systematic bias and random error of the observations caused by the

167 errors of numerical models and instruments are the key factors to directly assimilate

168 the satellite radiance data. Apart from eliminating cloud pixels, other procedures are

169 implemented inside the data assimilation framework for the quality control are as

170 follows. (1) when reading the data, remove the observed outliers with values below 50

171 K or above 550 K; (2) only the marine observations are applied by removing the

172 observations on the land and the observations over complex surfaces; (3) remove

173 observations when the observation minus the background is larger than 3 times of the

174 observation error; (4) the pixels are removed when the cloud liquid water path

175 calculated by the background field of the numerical model is greater than or equal to

176 0.2 kg/m2; (5) eliminate the data when the observation minus background is greater

177 than 5 K. These two parameters are used for these radiances on different sensors of

178 various satellites such as AMSU-A, MHS, and the Advanced Microwave Scanning

179 Radiometer 2 (AMSR2) (Wang et al., 2018, Yang et al., 2016).

180 By using 3DVAR algorithm, the assumption is that there is no bias between

181 observation and background (Dee et al., 2009; Liu et al., 2012; Zhu et al., 2014). A

182 bias correction scheme for observation is essential before DA. Usually, radiance bias

183 can be obtained by a linear combination of a set of forward operators.

184
$$\tilde{H}(x,\beta) = H(x) + \beta_0 + \sum_{i=1}^{N_p} \beta_i p_i \qquad (1)$$

185 Here, $H(x)$ represents the initial observation operator (before the bias

186 correction) and x represents the mode state vector. N_p is the number of the

187 predictiors. β_0 represents a constant component of the total bias (constant part),

188 while p_i and β_i represent the i-th predictor and its coefficient respectively. In this

189 study, four potentially state-dependent predictors (1000–300 hPa and 200–50 hPa

190 layer thicknesses, surface skin temperature, and total column water vapor) are applied.

191 The variational bias correction (VarBC) scheme is utilized to update the bias

192 correction coefficient variationally with the new observation operator considered in

193 the cost function of 3DVAR.

194 **3. Introduction to the typhoon and experimental design**

195 *3.1 Typhoon Soudelor*

196 From the record of the China Meteorological Administration (CMA), Typhoon

197 Soudelor was the 13th typhoon in 2015 as the second strongest tropical cyclone in that

198 year. At 1200 UTC 30 July 2015, it formed at northwest Pacific Ocean as a tropical

199 storm at 13.6° N, 159.2° E, then moved north-westwards. It upgraded to a strong

200 tropical storm at 2100 UTC 1 August 2015. Afterwards, it went through a process of

201 rapid intensification. It became a typhoon at 0900 UTC 2 August 2015, a strong

202 typhoon at 2100 UTC 2 August 2015, a super typhoon at 0900 UTC 3 August 2015.

203 Then it weakened to a strong typhoon in the morning on 5 August 2015. However, it

intensified to a super typhoon again at 1200 UTC 7 August 2015 with a maximum

surface wind of 52 m s^{-1}, moving west by north, and its intensity raised to its second

peak. It was reduced to a strong typhoon again at 1800 UTC 7 August 2015. It

decreased to a typhoon, entering to Taiwan Strait. It landed again as a typhoon at 1410

UTC on the coast of Fujian Province, China. Owing to continuous orographic friction,

it decreased to a tropical depression. Fig. 2 shows the track of Soudelor and different

color lines represent typhoon's maximum surface wind. It is displayed that after the

formation of typhoon, its track is relatively stable. After July 30, the tropical

depression moved west by north at a speed of about 20 km/h. Its moving tendency

changed slightly within 10 days of its generation. However, its intensity went through

a rapid intensification, a weakening, a second intensification, following by a

continuous weakening after landing on the China. Fig. 3 demonstrates the variation of

typhoon's intensity from 31 July 2015 to 5 August 2015. It is shown that typhoon's

maximum surface wind increased fast, while its minimum sea level pressure

decreased sharply. This was the stage of typhoon's rapid intensification. The periodf

rom 1 August 2015 to 3 August 2015 during its rapid intensification is selected.

3.2 Experimental design

    Two experiments are designed to investigate the effects of AHI radiance data

direct assimilation on the analysis and forecast of Typhoon Soudelor starting from

1800 UTC 1 August 2015 to 0000 UTC 3 August 2015. WRF 3.9.1 is employed as the

forecast model in this experiment. Arakawa C grid is used in the horizon with a 5 km

grid distance. As is known, Arakawa A grid is "unstaggered" by evaluating all quantities at the same point on each grid cell. The "staggered" Arakawa B-grid separates the evaluation of the velocities at the grid center and masses at grid corners. Arakawa C grid further separates evaluation of vector quantities compared to the Arakawa B-grid. Vertically, it has 41 eta levels using 10 hPa as its top with coarser vertical spacing for the higher levels. The center of the model domain is located at (17.5 °N, 140 °E) (Fig. 4). The initial condition and lateral boundary are provided by 0.5°×0.5° Global Forecasting System (GFS) reanalysis data. The following parameterization schemes are used: The following parameterization schemes are used: WDM6 microphysics scheme (Lim et al., 2010), Grell Devenyi cumulus parameterization scheme (Grell et al., 2002), Rapid Radiative Transfer Model (RRTM) longwave radiation scheme (Mlawer et al., 1997), shortwave radiation scheme (Dudhia et al., 1989), and YSU boundary layer scheme (Hong et al., 2006) .

The experimental procedures are illustrated by Fig. 5. Firstly, a 6-hour's spin-up conducted initialized from 1800 UTC 1 August 2015 to prepare the background field for the data assimilation at 0000 UTC 2 August 2015. The 6-hour spin-up period is commonly applied to initialize the typhoon or hurricane system the data assimilation experiments, although longer spin-up period is also acceptable to introduce more model errors in the background such as 12-hour or 24-hour. The first experiment is assimilating GTS (Global Telecommunications System) conventional data (including aircraft report, ship report, sounding report, satellite cloud wind data, ground station

246   data) only, which is called control experiment (CTNL). Another experiment is

247   configured with AHI radiance data assimilation (AHI_DA). AHI radiance data is

248   assimilated hourly further from 0000 UTC to 0600 UTC on 2 August 2015.

249   Afterwards, a 48 hours forecast is launched as the deterministic forecast. The

250   climatological background error (BE) statistics are estimated using the National

251   Meteorological Center (NMC) method. There are 5 control variables applied in this

252   study including U component, V component, full temperature, full surface pressure,

253   and pseudo-relative humidity. The observation error for each channel is estimated

254   based on the observed brightness temperature minus background brightness

255   temperature (OMB) from 0000 UTC on 1 August 2015 to 0000 UTC on 3 August

256   2015 every 6 hours.

257   Fig. 4 also shows the distribution of GTS observation data at the simulated

258   domain at 0000 UTC 2 August 2015. It is proved that raw radiance observations

259   thinned to a grid with 2–6 times of the model grid resolution are able to remove the

260   potential error correlations between adjacent observations (Schwartz et

261   al ., 2012; Xu et al ., 2015; Choi et al., 2017). Hence, 20 km is chosen to make

262   thinning of AHI radiance data. Also, sensitivity experiments with 25 km, and 30 km

263   thinning mesh are also conducted with similar results (Wang et al., 2018). The length

264   scale and the variance scale are set to be 0.5 and 1 respectively after several

265   sensitivity experiments conducted on tuning the background error. Similar

266   conclusions are also found in Shen and Min (2015) with the scale factors related to

267   the static background error covariance.

268   **4. Results**

269   *4.1 Minimization iterations*

270   In this study, minimization stops when the norm of the gradient for the cost

271   function is reduced by a factor of 0.01, which is commonly used in data assimilation

272   procedures. Inner minimization stops either when the criterion of the cost function

273   gradient is met or when inner iterations reach 200. Fig. 6 shows the cost function and

274   gradient with the iteration times. It is found that, for this case, the criterion of the cost

275   function gradient decrease is met. There is an obvious exponential decrease curve in

276   Fig. 6a, while Fig. 6b shows gradient decreases with the increase of iteration times. It

277   is seen from Fig. 6a that cost function decreases remarkably in the first 10 iterations.

278   However, after 30 times of iteration, the cost function curve becomes smooth

279   gradually. The differences between background field and observation were largest.

280   With continuous iterations, background field goes through continued adjustments.

281   Finally, the cost function tended to reach a stable minimum that represents the point

282   when cost function has its optimal solution. Besides, the gradient in Fig. 6b decreases

283   generally with increasing iterations. The exponential decrease of the cost function and

284   the change trend of its gradient indicate that the effectiveness of AHI radiance DA.

285   The final iterated analytical field was close to the observation. The wall clock times

286   used by CTNL and AHI_DA for the data assimilation procedures are rather

287   comparable with roughly 30 minutes and 40 minutes on a Linux workstation with 36

288   processors. It should be pointed out that computational cost of the deterministic

289   forecast and the pre-process for gribbed GFS data are same in these two experiments.

290   *4.2 Analytical results of the brightness temperature*

291   Figs. 7a, c, and, e show the distribution of OMB, while the observed brightness

292   temperature minus the simulated brightness temperature from the analyses (OMA)

293   after the bias correction of AHI radiance data are presented in Figs. 7b, d, and f from

294   channels 8, 9, and 10 at 0000 UTC 2 August 2015. It should be pointed that even only

295   parts of the AHI radiance data (roughly 20000 clear sky pixels of total 50000 pixels

296   for each DA cycle) are applied after quality control in the data assimilation, the

297   radiative transfer model is able to simulate the brightness temperature for all the

298   model grid point with the background and the analysis respectively for the verification

299   purpose. The similar verification method is also applied in Yang et al., (2016). In the

300   Fig. 7a, part of typhoon's spiral cloud belt was clearly visible. The brightness

301   temperature in typhoon's inner-core area was low, while the brightness temperature in

302   other areas was high. The mean of observed OMB was -4.65 K, indicating that the

303   background brightness temperature was higher than the observation. It is found in Fig.

304   7b that the OMA values of most pixels were below 0.02 K, indicating that the

305   analytical field fitting the observation after analyzing. It can be inferred from Figs. 7a,

306   c, and e that the magnitude in OMB of channel 10 was generally larger than that of

307   channel 9, while that of the OMB in channel 8 was the smallest. This is because the

308   detection height of channel 10 was lower than that of channel 8 and 9 seen from the

309 weighting function (Fig. 1), indicating channel 10 is largely affected by the clouds.

310 Conversely, the weighting peak of the channel 8 was the highest, being least affected

311 by the clouds. In general, the simulated brightness temperature from the analyses

312 matched well with the observed brightness temperature of all the three water vapor

313 channels after the assimilation of AHI radiance data.

314   To validate the effect of the bias correction for AHI radiance data at 0000 UTC 2

315 August 2015, the scatter plots of the observed brightness temperature and the

316 brightness temperature from the background before the bias correction are shown in

317 Figs. 8a, d, and g. Similarly, the results after the bias correction are provided in Figs.

318 8b, e, and h. From Fig. 8a, before the bias correction, the values from the observation

319 and the background were comparable, but most of the scatter points were below the

320 diagonal line. This suggests that the observed brightness temperature was higher than

321 the background simulated brightness temperature. From Fig. 8b, after the bias

322 correction, the observed warm bias was corrected to some extent with the root mean

323 square error (RMSE) of OMB decreasing from 1.864 K to 1.627 K and the average

324 decreasing from 0.956 K to 0.358 K. The scatter plots of the observed brightness

325 temperature and the brightness temperature from the analyses after the bias correction

326 are shown in Figs. 8 c, f, and j. Compared to the result of Fig. 8b, the scatters in Fig.

327 8c were more symmetrical, fitting closely to the diagonal line. The mean and RMSE

328 were also significantly reduced, suggesting that the analytical fields match better with

329 the observation than background field. Among them the RMSEs of channel 10 are

330 smallest compared to those from channels 8 and 9 for the OMB and OMA samples,

331 which is likely related to strict cloud detection scheme for channel 10 with rather

332 lower detecting peak (Wang et al., 2018).

333   Fig. 9 shows the observation numbers, the mean, and the standard deviation of

334 OMB and OMA of channels 8, 9, and 10 before and after the bias correction. It can be

335 seen that after the quality control, 24057, 24181, 21785 observations are adopted in

336 the DA system for channels 8, 9, and 10, respectively. From the mean value of OMB

337 before the bias correction, the value of the three channels was relatively small,

338 indicating that the simulated brightness temperature of the three channels was close to

339 the observed brightness temperature. The lowest mean of 0.3 K was found in channel

340 10, indicating that the simulated brightness temperature of channel 10 was closest to

341 the observed brightness temperature. Bias correction effectively corrected the

342 systematic bias and reduces the mean value of observation residuals. After the bias

343 correction, the OMB mean value of the three channels significantly decreases to

344 nearly 0 K. With the bias correction, the simulated brightness temperature was almost

345 the same as the observed brightness temperature. The standard deviations (stdv) of

346 OMB were comparable before and after the bias correction, since they are calculated

347 by subtracting the mean of the bias. It is found that the bias was corrected effectively

348 with an overall same magnitude of bias for each pixel, leading the stdv almost same

349 before and after the bias correction. The standard deviation of OMA decreased by

350 about 80% compared to OMB, indicating that the analyses fit better with the

351 observations after the data assimilation. Differences between the standard deviations

352 of the OMB and OMA were statistically significant at the 95% level using zero

353 difference for the null hypothesis.

354   The RMSEs of the simulated brightness temperature by the NWP model before

355 and after the assimilation are also calculated against the AHI radiance observations.

356   Fig. 10 shows the RMSEs during the DA cycles for channels 8, 9, and 10. As can be

357   seen from Fig. 10, RMSE decreased after each analysis in AHI_DA. The most

358   significant improvement was from the first analysis cycle of channel 8, where RMSE

359   of the brightness temperature after assimilation significantly decreases from 1.64 K to

360   0.46 K, possibly due to the largest adjustment on the background for the first analysis

361   time. The background before the assimilation was the short-term forecast from the

362   previous analysis. The increase of the RMSE in the fluctuation arised from the model

363   error in the 1 hour short-term forecast. Overall, the effect of the analysis from the

364   channel 10 was most significant.

365   *4.3 Analysis of the typhoon structure*

366   Fig. 11 shows the wind field at sea level and the distribution of water vapor at

367   850 hPa at 0000 UTC 2 August 2015. The obvious cyclonic eddy circulation

368   structures in the core area of the typhoon are found in both fields, while the

369   anti-cyclonic circulation existed in the northwest quadrant of the typhoon. The mixing

370   ratio of water vapor in the region where the typhoon located was very high and the

371   wind field is cyclonic, indicating that the typhoon has a continuous water vapor

372   advection. This contributed to the enhancement of typhoon (Kamineni, et al., 2003).

373   From the flow field of the control experiment in Fig. 11a, the water vapor

374   convergence in the center of the typhoon region was weak with the low intensity and

375   smaller coverage. As can be seen from Fig. 11b, after the assimilation of AHI radiance

376   data, the streamlines in the typhoon region become denser, indicating that the cyclonic

377 circulation was strengthened. Conversely, the intensity and distribution of the water

378 vapor after the assimilation of AHI radiance data tend to contribute to the developing

379 typhoon. This suggests that the field outside of the typhoon center was also adjusted

380 as the assimilation of AHI radiance data was able to improve the large-scale

381 environmental field in the simulation region of Typhoon Soudelor. It should be

382 pointed out that the model status in the cloudy area was modified due to the spatial

383 correlation in the background error covariance. The similar findings for small-scale

384 information in the cloudy area can also be referred in Wang et al., (2018).

385 *4.4 Track forecast*

386   In order to further evaluate the effect of AHI radiance data assimilation, a 48-hour

387 deterministic forecast was launched with the analyses initialized from 0000 UTC 2

388 August 2015 and 0600 UTC 2 August 2015 respectively. The best track data are

389 provided by the CMA (Yu et al., 2007; Song et al., 2010). The improvement is most

390 obvious at the start and end point. As can be seen in Fig. 12a, at the beginning of the

391 forecast, the initial location of the typhoon from the CTNL experiment has large south

392 bias and east bias at 0000 UTC and 0600 UTC respectively. Conversely, the location

393 of the typhoon in AHI_DA is relatively closer to the observation at the beginning..

394 During the following few hours of forecasts, the typhoon track predicted by the CTNL

395 continues to show a south-west bias with the environmental wind, while the track

396 predicted by AHI_DA match better with the best track. Fig. 12c shows the averaged

397 typhoon track error over the two forecasts predicted by the two experiments. At the

initial time of the forecast, the track errors of CTNL and AHI_DA were significantly

different, with the magnitude of 55.6 km and 13.4 km, respectively. During the

subsequent 48-hour forecast, the track error of the CTNL gradually increases with the

forecast time reaching 167.1 km at the end of the forecast. In contrast, the track error

of AHI_DA is consistently less than 122.5 km during the 48-hour forecast period. In

general, the average track error of the CTNL is 168.57 km, and the average track error

of AHI_DA experiment is only 67.0 km, indicating a significant improvement in the

track prediction.

Fig. 13 provides the time series of the typhoon intensity from the two

experiments in terms of the averaged maximum surface wind and minimum sea level

pressure error over the two forecasts initialized from 0000 UTC 2 August 2015 and

0600 UTC 2 August 2015 respectively. It can be seen that the maximum surface wind

error predicted by the AHI_DA was much lower than that by the CTNL for the first 30

hours, due to the overall under estimation for the intensity of Typhoon Soudelor

simulated in the background field. The maximum surface wind errors of AHI_DA are

generally smaller than those of CTNL. It should be pointed out that the difference

between the maximum surface wind errors of the two experiments reaches up to 7.5 m

s-1 after 24-hour forecast. In Fig. 13b, the results of the minimum sea level pressure

are consistent with Fig. 13a, while the improvement for the minimum sea level

pressure lasts for 40 hours.

5. Conclusion

An interface for AHI radiance data assimilation on the WRFDA system based on the 3DVAR assimilation method was built. Based on the Typhoon Soudelor in 2015, two experiments for comparison was designed to examine the impact of AHI water vapor channel radiance data assimilation on the analysis and prediction of the rapid development stage of Typhoon Soudelor under clear sky condition. Following conclusions are obtained:

(1) The AHI radiance data on the new generation of geostationary meteorological satellite is able to reflect the structure of Typhoon Soudelor very clearly. After a series of pre-procedures such as the quality control, the bias correction, cloudy pixels are able to effectively be eliminated, ensuring the validity and rationality of the Ahi radiance data. The biases are also eliminated from the VarBC statistical method, which is able to provide a positive impact on the data assimilation procedure for the typhoon numerical simulation.

(2) Compared with the control experiment with only GTS data, the 3DVAR assimilation including AHI radiance data is able to improve the structure of typhoon's core and outer rain band. Also, the position and intensity of typhoon in the background field are able to be corrected.

(3) Generally, the track and minimum sea level pressure from the AHI radiance data assimilation experiment match better with the best track than the control experiment does for the subsequent 48-hour forecast. The maximum surface wind forecast error is

439 reduced only for the first 30-hour.

440 In this study, the AHI water radiance data assimilation is conducted under the

441 clear sky condition. The results of the experiments indicate that AHI radiance data

442 assimilation has a positive effect on the analysis and prediction of rapidly intensifying

443 TC. Although, the whole developing stages of Typhoon Soudelor include a rapid

444 intensification, a weakening, a second intensification, only the first intensification

445 during 1 August to 4 August considered as the numerical period. It is worth

446 investigating the impact of AHI data assimilation on the whole period including the

447 first intensification, a weakening, and the second intensification of Typhoon Soudelor

448 to fully prove the advantages of AHI radiance data assimilation. Considering the

449 complex influence of underlying surface, only the rapid development stage of typhoon

450 at sea were studied, while the whole generation, development and disappearance stage

451 of typhoon can also be studied in the future. In addition, based on the AHI radiance

452 data of the water vapor channels under the condition of clear sky, only 3DVAR

453 method was adopted. Further improvements under the condition of all sky and hybrid

454 DA can be obtained in the future.

455 **Acknowledgments**

456 This research was primarily supported by the Chinese National Natural Science

457 Foundation of China (G41805016), the Natural Science Foundation of Jiangsu

458 Province (BK20170940), the Chinese National Natural Science Foundation of China

459 (G41805070), the Chinese National Key R&D Program of China (2018YFC1506404,

460   2018YFC1506603), the research project of Heavy Rain and Drought-Flood Disasters

461   in Plateau and Basin Key Laboratory of Sichuan Province in China (SZKT201901,

462   SZKT201904), the research project of the Institute of Atmospheric Environment,

463   China Meteorological Administration, Shenyang in China (2020SYIAE07,

464   2020SYIAE02).

465

References

467   Bauer, P., Geer, A.J., Lopez, P., and Salmond, D.: Direct 4D–Var assimilation of

468   all-sky radiance. Part I: Implementation, Quarterly Journal of the Royal

469   Meteorological Society, 136, 1868-1885, 2010.

470   Bauer, P., Auligné, T., Bell, W., Geer, A., Guidard, V., Heilliette, S., et al: Satellite

471   cloud and precipitation assimilation at operational NWP centres, Quarterly Journal of

472   the Royal Meteorological Society, 137, 1934-1951, 2011.

473   Bessho, K., Date, K., Hayashi, M., Ikeda, A., Imai, T., Inoue, H., et al.: An

474   introduction to Himawari-8/9—Japan's new-generation geostationary meteorological

475   satellites, Journal of the Meteorological Society of Japan, 94, 151-183, 2016.

476   Buehner, M., Caya, A., Carrieres, T., and Pogson, L.: Assimilation of SSMIS and

477   ASCAT data and the replacement of highly uncertain estimates in the Environment

478   Canada Regional Ice Prediction System, Quarterly Journal of the Royal

479   Meteorological Society, 142, 562-573, 2016.Choi, Y., Cha, D.-H., Lee, M.-I., Kim,

J., Jin, C.‐S., Park, S.‐H., and Joh, M.‐S.: Satellite radiance data assimilation for binary tropical cyclone cases over the western North Pacific, J. Adv. Model. Earth Syst., 9, 832-853, 2017.

Dee, D.P., and Uppala, S.: Variational bias correction of satellite radiance data in the ERA–Interim reanalysis, Quarterly Journal of the Royal Meteorological Society, 135, 1830-1841, 2009.

DeMaria, M., Sampson C.R., Knaff J.A., and Musgrave K.D.: Is tropical cyclone intensity guidance improving? Bulletin of the American Meteorological Society, 95, 387-398, 2014.

Derber, J.C., and Wu, W.S.: The use of TOVS cloud–cleared radiance in the NCEP SSI analysis system, Mon. Wea. Rev, 126, 2287-2299, 1998.

Di, D., Ai, Y., Li, J., Shi, W., and Lu, N.: Geostationary satellite-based 6.7 μm band best water vapor information layer analysis over the Tibetan Plateau, Journal of Geophysical Research: Atmospheres, 121, 4600-4613, 2016.

Dudhia, J.: Numerical Study of Convection Observed during the Winter Monsoon Experiment Using a Mesoscale Two-Dimensional Model, Journal of the Atmospheric Sciences, 46, 3077-3107, 1989.

Geer, A. J., Baordo, F., Bormann, N., English, S., Kazumori, M., Lawrence, H., Lean, P., Lonitz, K., and Lupu, C.: The growing impact of satellite observations sensitive to humidity, cloud and precipitation, Quart. J. Roy. Meteorol. Soc., 143, 3189-3206.

Goodman, S.J., Gurka, J., DeMaria, M., Schmit, T.J., Mostek, A., Jedlovec, G., et al.:

The GOES-R proving ground: Accelerating user readiness for the next-generation geostationary environmental satellite system, Bulletin of the American Meteorological Society, 93, 1029-1040, 2012.

Grell G.A., Dévényi D.: A generalized approach to parameterizing convection combining ensemble and data assimilation techniques, Geophys. Res. Let., 29, 587-590, 2002.

Hilton, F., Atkinson, N. C., English, S. J., and Eyre, J. R.: Assimilation of IASI at the Met Office and assessment of its impact through observing system experiments, Quarterly Journal of the Royal Meteorological Society, 135, 495-505, 2009.

Hong S.Y., Noh Y., Dudhia J.: A New Vertical Diffusion Package with an Explicit Treatment of Entrainment Processes. Mon. Wea. Rev, 134, 2318-2341, 2006.

Jung, J.A., Zapotocny, T.H., Le Marshall, J.F., and Treadon, R.E.: A two-season impact study on NOAA polar-orbiting satellites in the NCEP Global Data Assimilation System, Weather Forecasting, 23, 854-877, 2008.

Kamineni, R., Krishnamurti, T., Ferrare, R., Ismail, S., and Browell, E.: Impact of high resolution water vapor cross-sectional data on hurricane forecasting, Geophysical Research Letters, 30, 38-1, 2003.Kazumori, M.: Satellite radiance assimilation in the JMA operational mesoscale 4DVAR system, Mon. Wea. Rev, 142, 1361-1381, 2014.

Li, X., and Zou, X.: Bias characterization of CrIS radiances at 399 selected channels with respect to NWP model simulations, Atmospheric Research, 196, 164-181, 2017.

521 Lim, K.-S. S., and Hong, S.-Y.: Development of an effective double-moment cloud

522 microphysics scheme with prognostic cloud condensation nuclei (CCN) for weather

523 and climate models. Mon. Wea. Rev, 138, 1587-1612, 2010.

524 Liu, Z., Schwartz, C.S., Snyder, C., and Ha, S.Y.: Impact of assimilating AMSU-A

525 radiance on forecasts of 2008 Atlantic tropical cyclones initialized with a limited-area

526 ensemble Kalman filter, Mon. Wea. Rev,, 140, 4017-4034, 2012.

527 Liu, Q., and Weng, F.: Advanced doubling-adding method for radiative transfer in

528 planetary atmosphere. J. Atmos. Sci., 63, 3459–3465, 2006.

529 Ma, Z., Maddy E.S., Zhang B., Zhu T., and Boukabara S.A.: Impact Assessment of

530 Himawari-8 AHI Data Assimilation in NCEP GDAS/GFS with GSI, J. Atmos.

531 Oceanic Technol., 34, 797-815, 2017.

532 McNally, A.P., Watts, P.D., Smith, J.A., Engelen, R., Kelly, G.A., Thépaut, J.N.,

533 and Matricardi, M.: The assimilation of AIRS radiance data at ECMWF, Quarterly

534 Journal of the Royal Meteorological Society, 132, 935-957, 2006.

535 Minamide, M., and Zhang F.: Assimilation of all-sky infrared radiances from

536 himawari-8 and impacts of moisture and hydrometer initialization on

537 convection-permitting tropical cyclone prediction. Mon. Wea. Rev, 146, 3241-3258,

538 2018.

539 Mlawer E.J., Taubman S.J., Brown P.D., et al.: Radiative transfer for inhomogeneous

540 atmospheres: RRTM, a validated correlated-k model for the longwave, Journal of

541   Geophysical Research Atmospheres, 102, 16663-16682, 1997.

542   Montmerle, T., Rabier, F., and Fischer, C.: Relative impact of polar–orbiting and

543   geostationary satellite radiance in the Aladin/France numerical weather prediction

544   system, Quarterly Journal of the Royal Meteorological Society, 133, 655-671, 2007.

545   Noh Y., Cheon W.G., Hong S.Y., et al.: Improvement of the K-profile Model for the

546   Planetary Boundary Layer based on Large Eddy Simulation Data, Boundary-Layer

547   Meteorology, 107, 401-427, 2003.

548   Prunet, P., Thépaut, J.N., Cassé, V., Pailleux, J., Baverez, A., and Cardinali,

549   C.: Strategies for the assimilation of new satellite measurements at Météo–

550   France, Advances in Space Research, 25, 1073-1076, 2000.

551   Qin, Z., Zou, X., Weng, F.: Evaluating Added Benefits of Assimilating GOES Imager

552   Radiance Data in GSI for Coastal QPFs, Mon. Wea. Rev, 141, 75-92, 2013.

553   Rennie, M.P.: The impact of GPS radio occultation assimilation at the Met

554   Office, Quarterly Journal of the Royal Meteorological Society, 136, 116-131, 2010.

555   Schmit, T.J., Gunshor, M.M., Paul Menzel, W., Gurka, J., Li, J., and Bachmeier,

556   S.: Introducing the next–generation advanced baseline imager (ABI) on

557   GOES-R, Bulletin of the American Meteorological Society, 86, 1079-1096, 2005.

558   Schmit, T.J., Li, J., Li, J., Feltz, W.F., Gurka, J.J., Goldberg, M.D., and Schrab,

559   K.J.: The GOES-R Advanced Baseline Imager and the continuation of current sounder

560   products, Journal of Applied Meteorology and Climatology, 47, 2696-2711, 2008.

Schmit, T.J., Griffith, P., Gunshor, M.M., Daniels, J.M., Goodman, S.J., and Lebair, W.J.: A closer look at the ABI on the GOES-R series, Bulletin of the American Meteorological Society, 98, 681-698, 2017.

Schwartz, C. S., Liu, Z., Chen, Y. and Huang X.-Y.: Impact of assimilating microwave radiances with a limited‐area ensemble data assimilation system on forecasts of Typhoon Morakot, Weather Forecasting, 27, 424-437, 2012.

Shen, F., and Min, J.: Assimilating AMSU-A radiance data with the WRF hybrid En3DVAR system for track predictions of Typhoon Megi (2010), Advances in Atmospheric Sciences, 32, 1231-1243, 2015.

Song J-J, Wang Y, Wu L.: Trend discrepancies among three best track data sets of western North Pacific tropical cyclones. J. Geophys. Res. 115: D12128, DOI: 10.1029/2009JD013058, 2010.

Stengel, M., Undén, P., Lindskog, M., Dahlgren, P., Gustafsson, N., and Bennartz, R.: Assimilation of SEVIRI infrared radiance with HIRLAM 4D-Var, Quarterly Journal of the Royal Meteorological Society, 135, 2100-2109, 2009.

Wang, Y., Liu, Z., Yang, S., Min, J., Chen, L., Chen, Y., and Zhang, T.: Added value of assimilating Himawari-8 AHI water vapor radiances on analyses and forecasts for "7.19" severe storm over north China, Journal of Geophysical Research: Atmospheres, 123, 3374-3394, 2018.

Xu, D., Liu, Z., Huang, X.-Y., Min, J., and Wang, H.: Impact of assimilation IASI

radiances on forecasts of two tropical cyclones, Meteorology and Atmospheric Physics, 122, 1-18, 2013.

Xu, D., Huang, X.-Y., Wang H., Mizzi, A. P. and Min J.: Impact of assimilating radiances with the WRFDA ETKF/3DVAR hybrid system on prediction of two typhoons in 2012, J. Meteorol. Res, 29, 28-40, 2015.

Yan, B., Weng, F., and Derber, J. Assimilation of satellite microwave water vapor sounding channel data in NCEP Global Forecast System (GFS), paper presented at 17th International TOVS Study Conference, Int. ATOVS Working Group, Monterrey, Calif, 2010.

Yang, C., Liu, Z., Bresch, J., Rizvi, S. R. H, Huang, X.-Y., and Min, J.: AMSR2 all-sky radiance assimilation and its impact on the analysis and forecast of Hurricane Sandy with a limited-area data assimilation system, Tellus A: Dynamic Meteorology and Oceanography, 68, 2016.

Yu H, Hu C, Jiang L.: Comparison of three tropical cyclone intensity datasets. Acta Meteorol. Sin. 21, 121-128, 2007.

Zapotocny, T.H., Jung, J.A., Le Marshall, J.F., and Treadon, R.E.: A two–season impact study of satellite and in situ data in the NCEP Global Data Assimilation System, Weather Forecasting, 22, 887-909, 2007.

Zhu, Y., Derber, J., Collard, A., Dee, D., Treadon, R., Gayno, G., and Jung, J.A.: Enhanced radiance bias correction in the National Centers for Environmental Prediction's Gridpoint Statistical Interpolation data assimilation system, Quarterly

602   Journal of the Royal Meteorological Societ, 140, 1479-1492, 2014.

603   Zou, X., Qin, Z., and Weng, F.: Improved coastal precipitation forecasts with direct

604   assimilation of GOES-11/12 imager radiance, Mon. Wea. Rev, 139, 3711-3729, 2011.

605   Zou, X., Qin Z., and Zheng Y.: Improved tropical storm forecasts

606   with GOES-13/15 imager radiance assimilation and asymmetric vortex initialization

607   in HWRF, Mon. Wea. Rev, 143, 2485-2505, 2015.

608

609

610   **List of Figures**

611

612
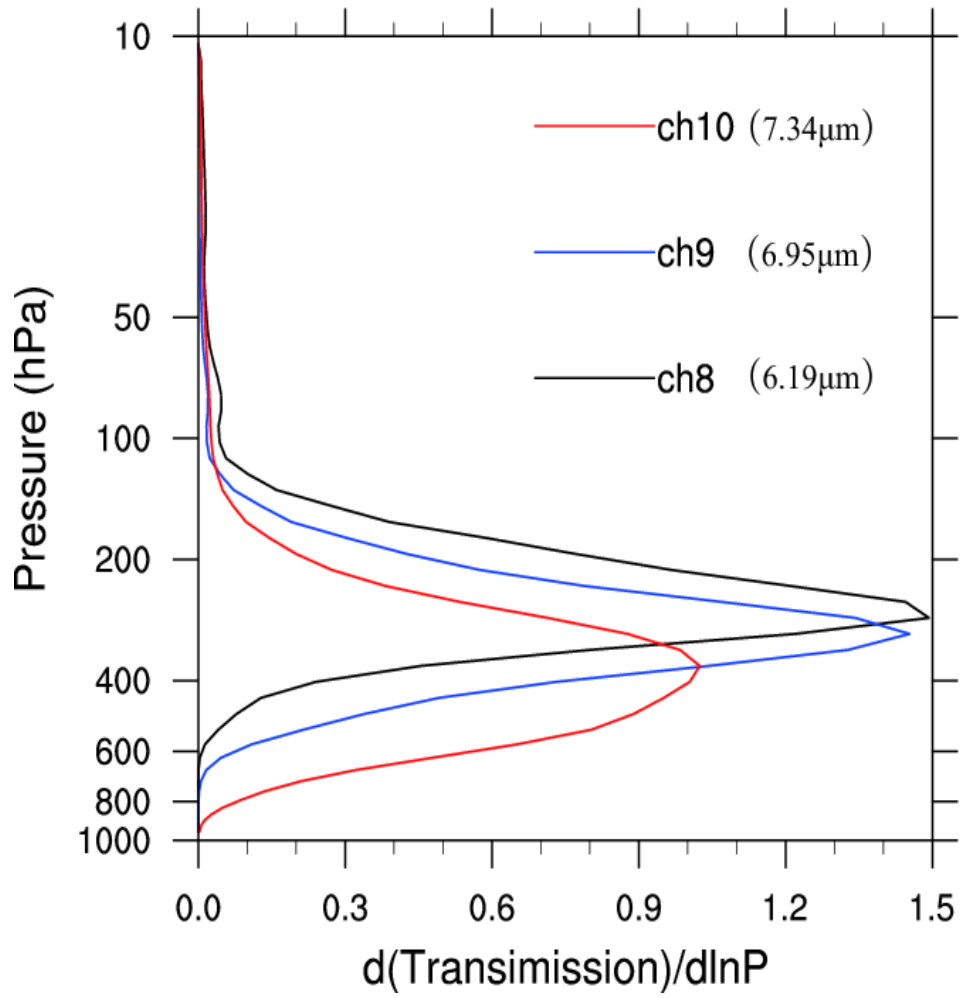
Fig.1 Weighting functions of Himawari-8 Advanced Himawari Imager three water

vapor channels for Channel 8, 9, and 10.

613

614

615

616

617

618
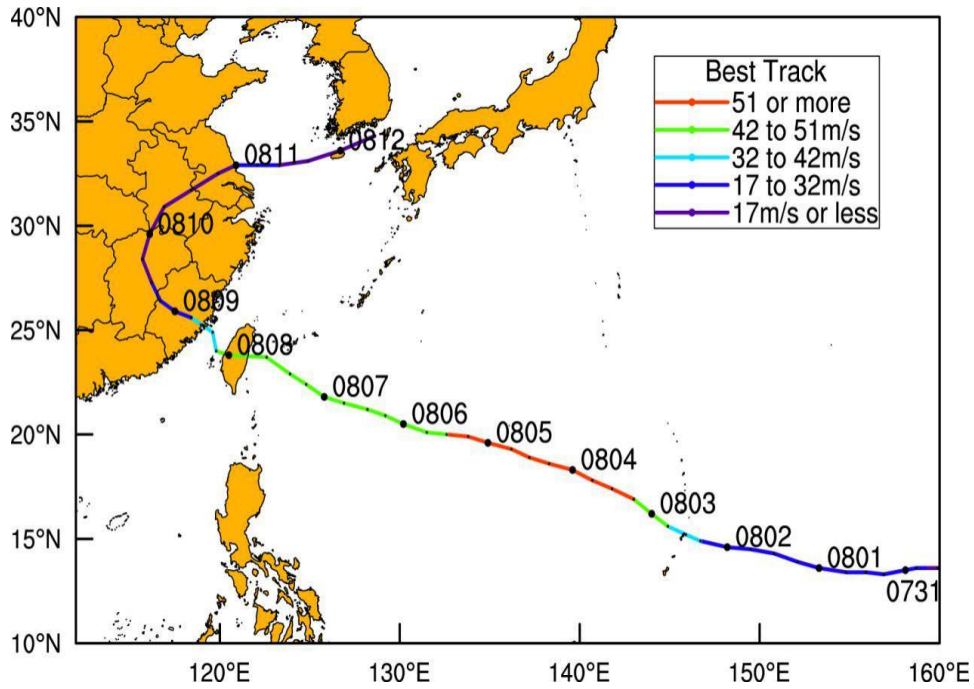
619

620 Fig.2 The best track of Soudelor from the China Meteorological Administration

621 (CMA) from 0000 UTC 30 July to 0600 UTC 12 August 2015. Different colors

622 represent intensity changes.

623

624

625

626

627

628

629

630
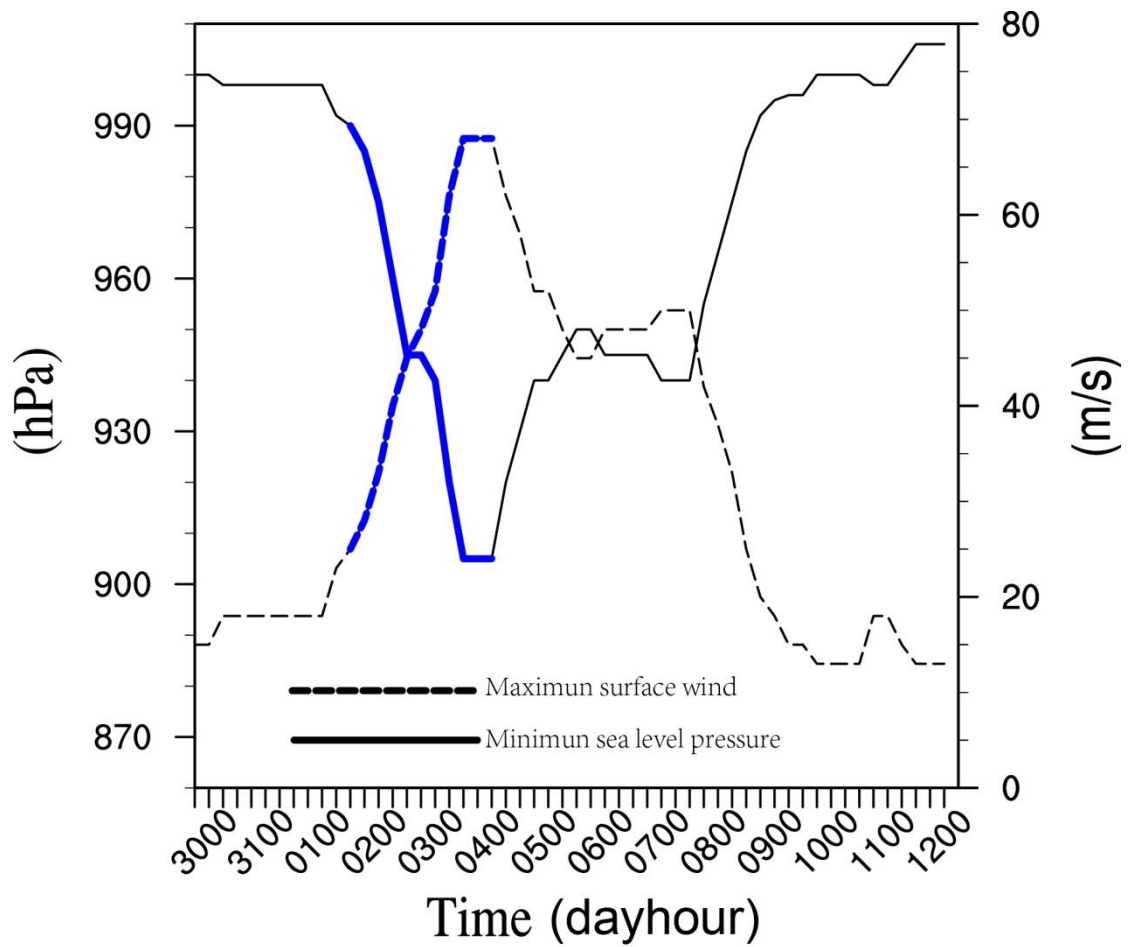
Fig. 3 The time series of the minimum sea level pressure (solid line, unit: hPa) and the

maximum surface wind (dash line, unit: m s^{-1}) of Typhoon Soudelor from the CMA

best-track data from 0000 UTC 30 July 2015 to 0600 UTC 12 August 2015. The

specific period for the numerical results from 1800 UTC 1 August 2015 to 0600 UTC

4 August 2015 is highlighted in blue.

636

637

638

639

640

641

642
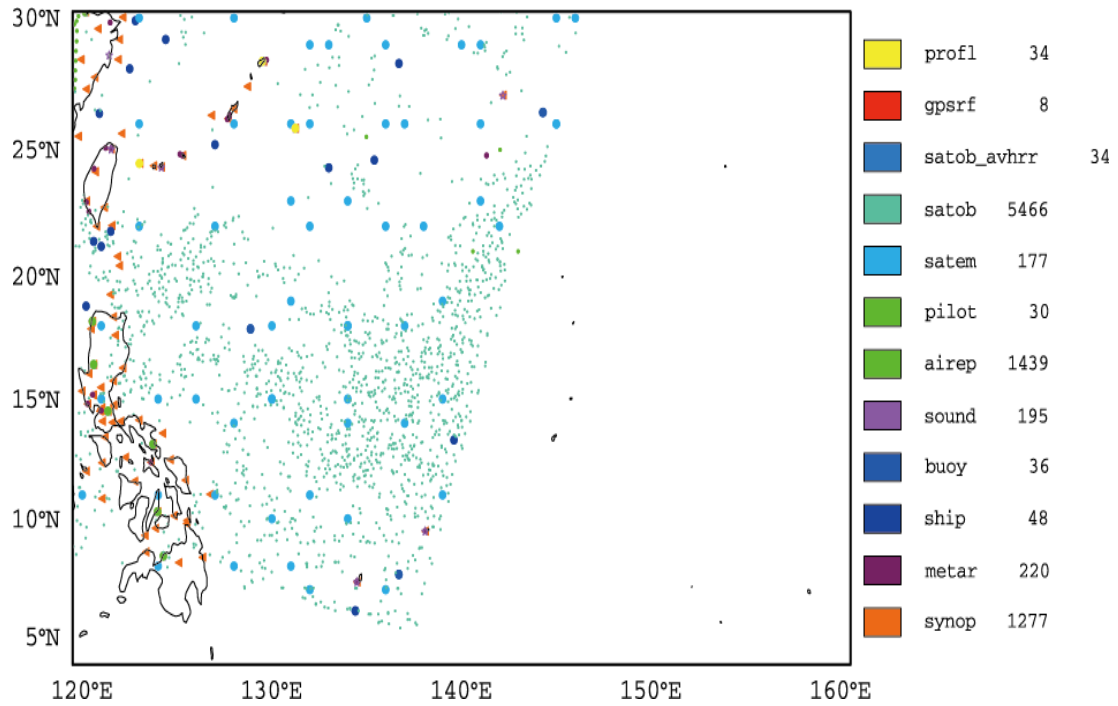
Fig. 4 Distribution of GTS observations in the simulated area at 0000 UTC 2 August

2015. On the right side of the map is the name of observation data and the number of

observations. Each observation type is marked with different color along with a

unique symbol.

647

648

649

650

651

652

653
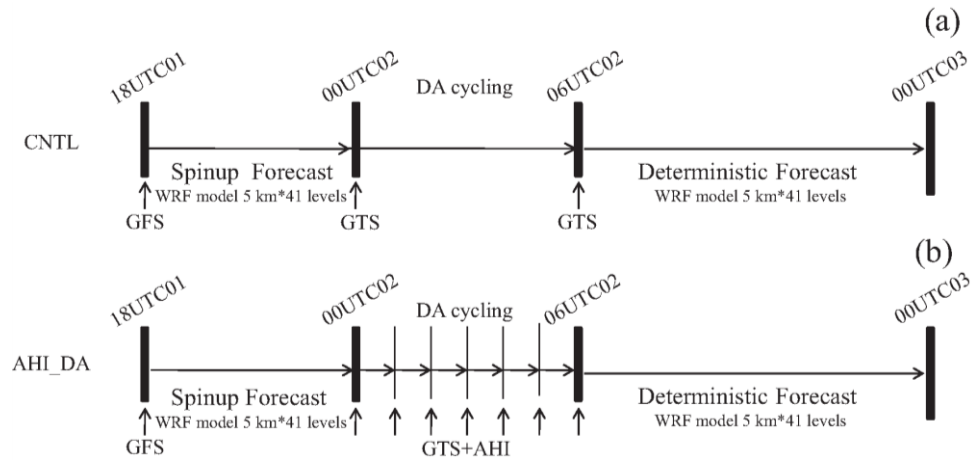
Fig. 5 The flow chart of the data assimilation experiments. (a) CTNL, (b) AHI_DA

656

657

658

659

660

661

662

663

664

665

666
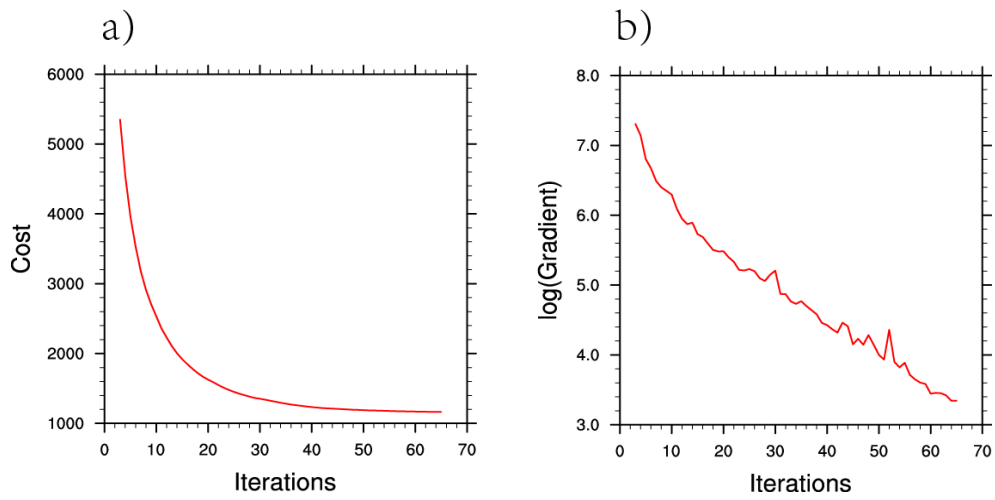
667

668   Fig. 6 (a) Cost function as functions of iterations, (b) gradient as functions of

669   iterations.

670

671

672

673

674

675

676

677

678

679

ch8(6.19μm)

680

ch9(6.95 μm)

681

ch10 (7.34 μm)

682
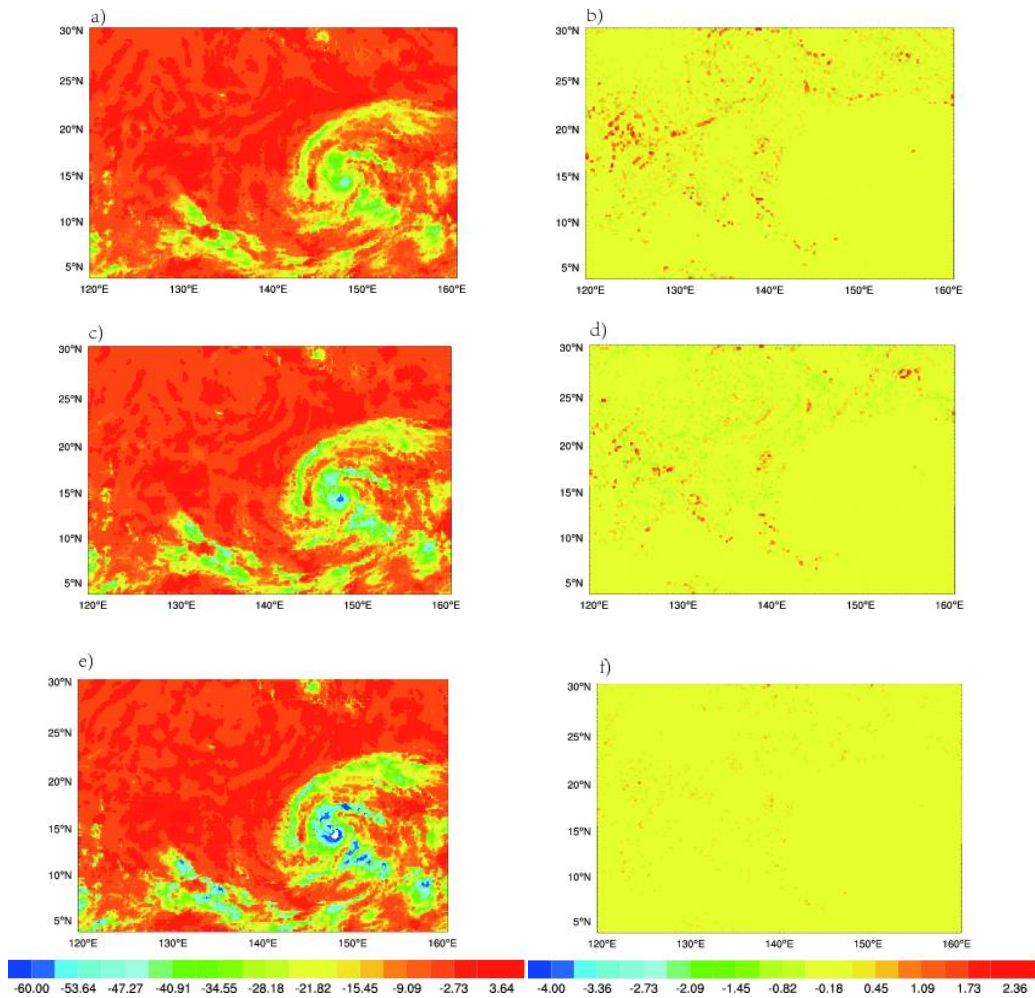
683   Fig. 7 (a, c, and e) OMB (unit: K) after bias correction for channel 8, 9, and 10,

684   respectively; (b, d, and f) OMA (unit: K) after bias correction for channel 8, 9, and 10,

685   respectively at 0000 UTC 2 August 2015.

686

687

688

689

690

691
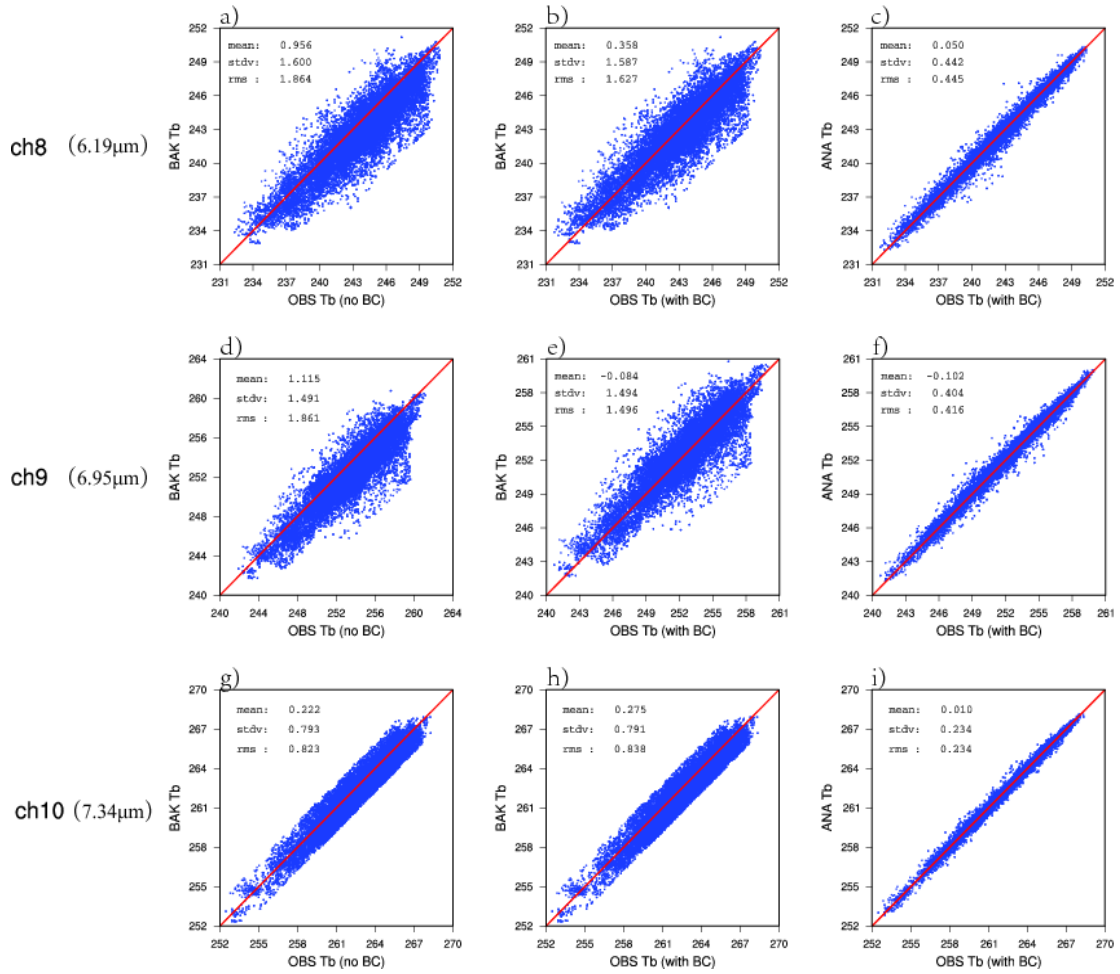
Fig. 8 Scatter plots of (a, d and g) the observed and background brightness temperature before the bias correction of channel 8, 9 and 10. Scatter plots of (b, e and h) the observed and background brightness temperature after the bias correction of channel 8, 9 and 10. Scatter plots of (c, f and i) the observed and analyzed brightness temperature after the bias correction of channel 8, 9 and 10.

697
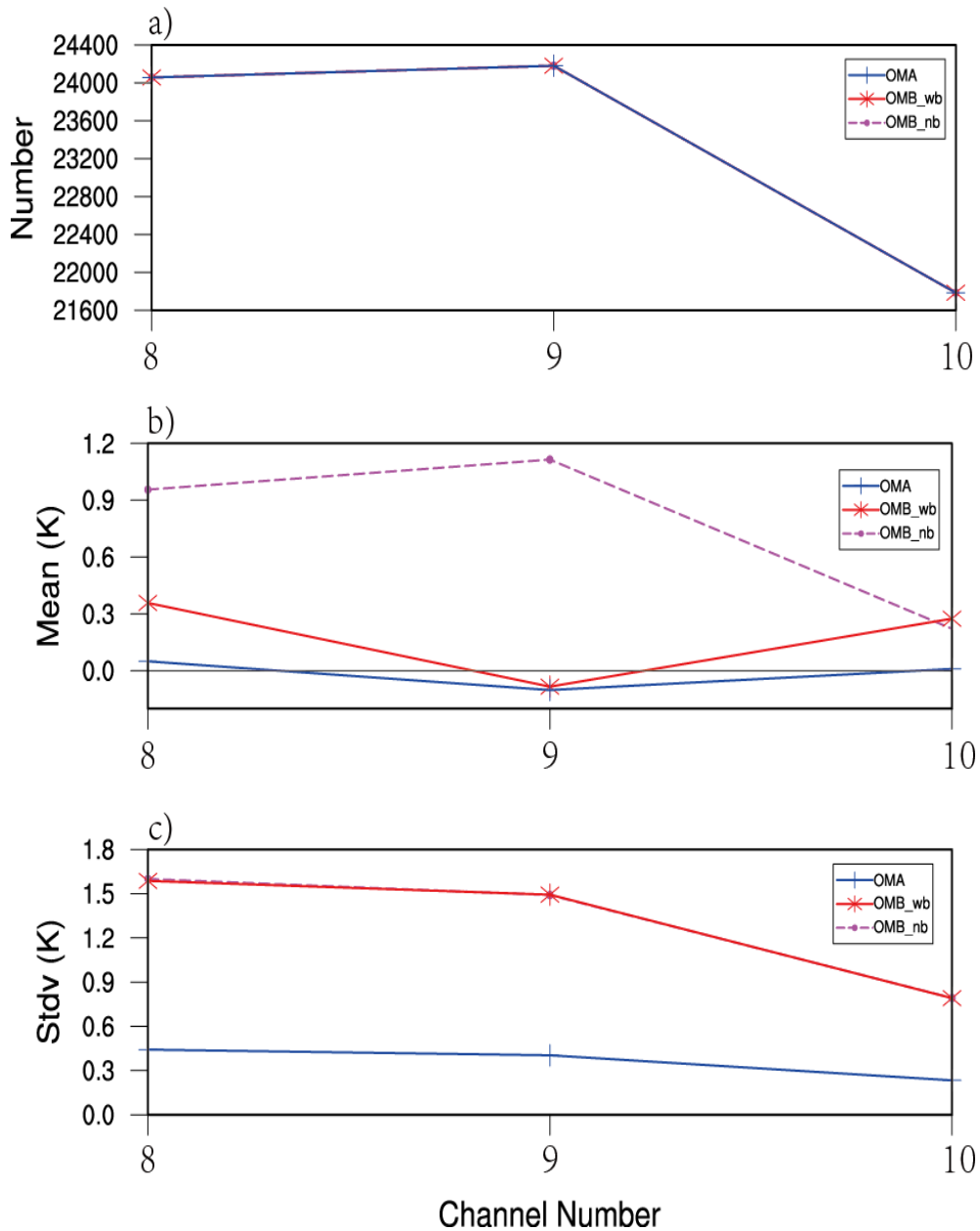
Fig. 9 Number of (a) observations, (b) mean (unit: K), and (c) standard deviations

(unit: K) of OMB and OMA before and after the bias correction for water vapor

channels 8-10 (OMB_nb: OMB without bias correction; OMB_wb: OMB with bias

correction).

702
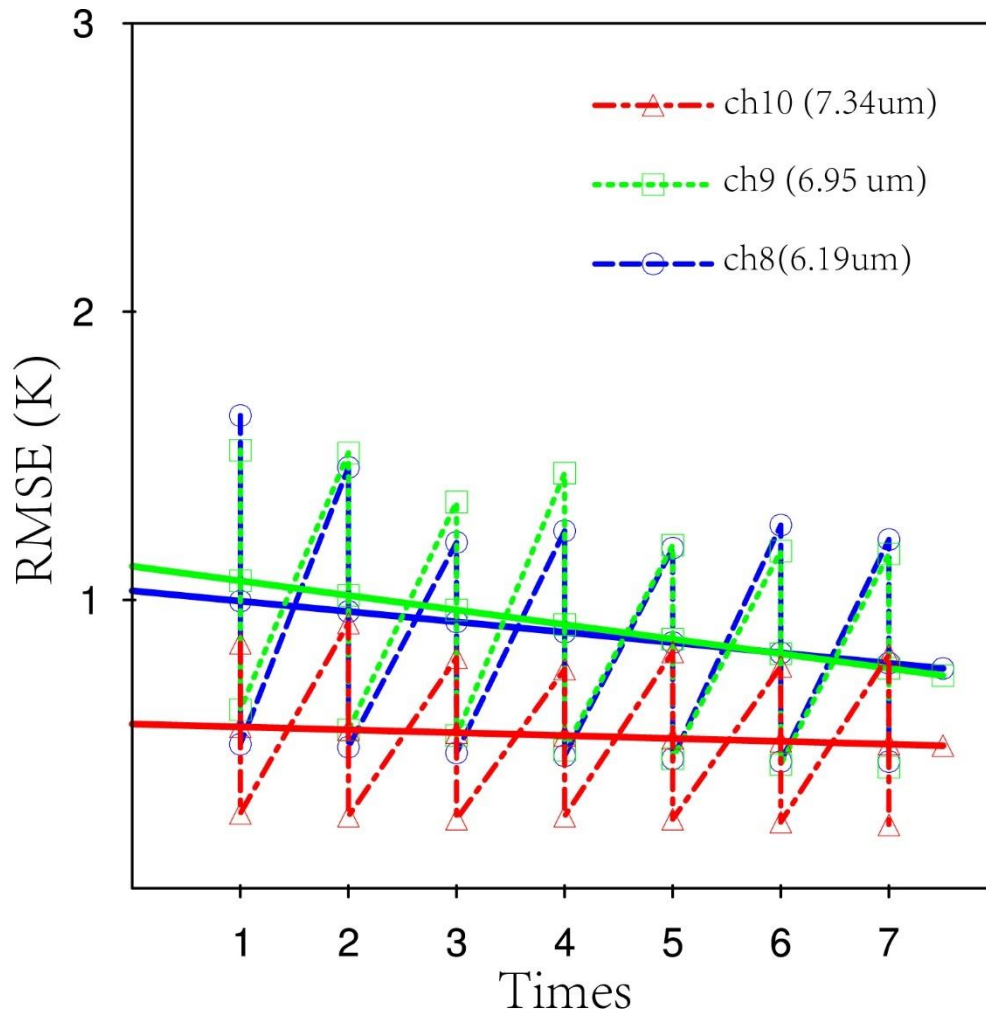
703

704   Fig.10 Time series of the RMSE for the brightness temperature (unit: K) with

705   assimilation times before and after the data assimilation along with the trend lines.

706

707

708

709

710

711

712
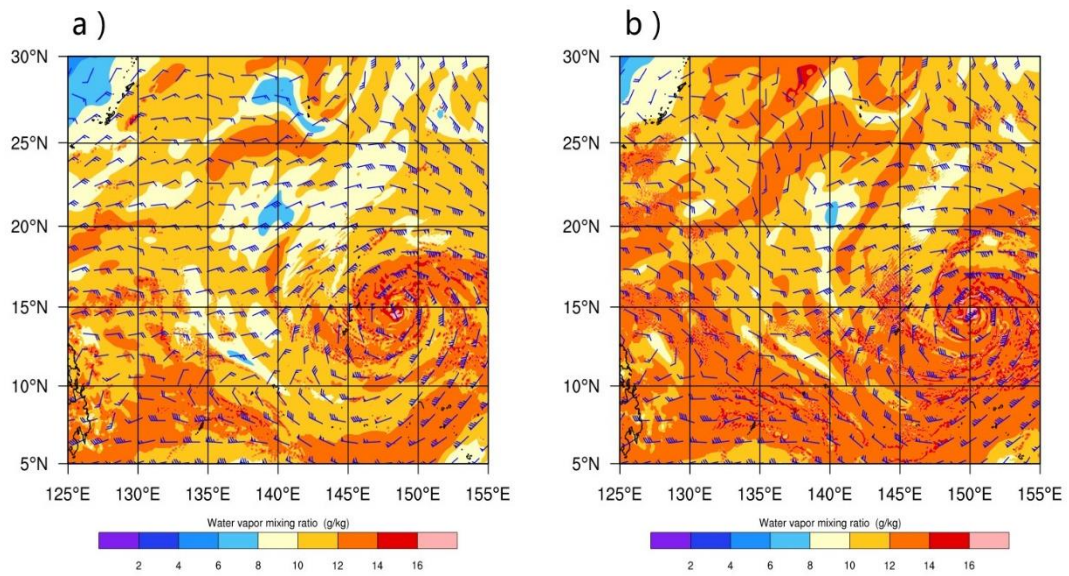
Fig. 11 The surface wind speed (vectors, unit: m s^{-1}) and water vapor (colored, unit:

g/kg) for (a) CTNL; (b) AHI_DA at 850 hPa at 0000 UTC 2 August 2015.

715

716

717

718

719

720

721

722

723

724

725
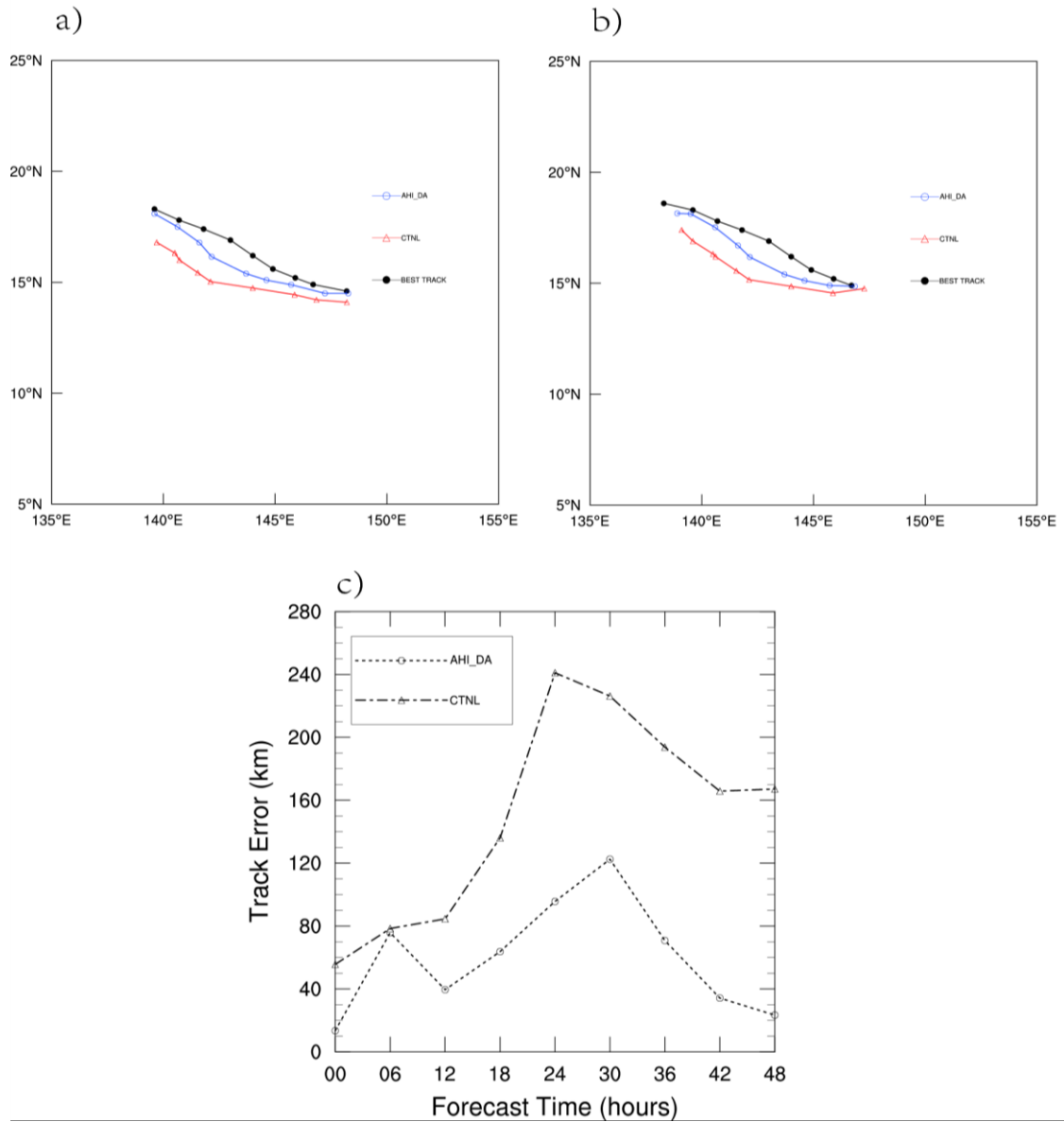
Fig. 12 The 48-hour predicted tracks (a) from 0000 UTC 2 August to 0000 UTC 4

August, (b) from 0600 UTC 2 August to 0600 UTC 4 August 2015, (c) averaged track

errors (unit: km) for the two forecasts.

729

730

731
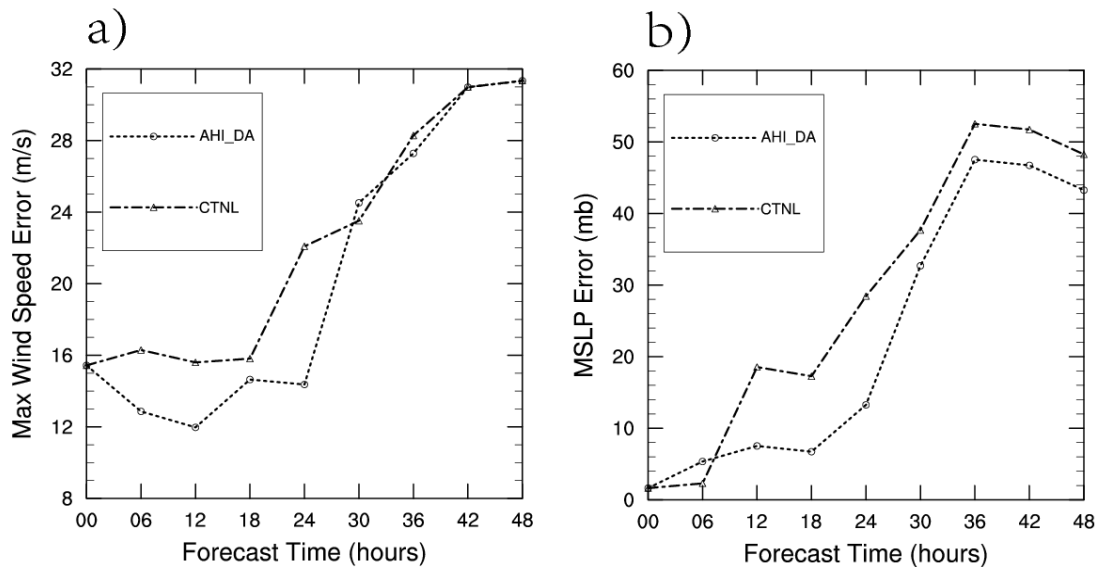
732

733   Fig.13 The 48-hour (a) maximum surface wind error (unit: m s^{-1}),(b) minimum sea

734   level pressure error (unit: hPa) of Soudelor (2015) averaged from two forecasts.

735

736

737

738

739

740

741

742

743

744 Code/Data availability. The WRF Model code used in this research is available at

745 https://www2.mmm.ucar.edu/wrf/users/download/get_source.html. The Himawari-8

746 AHI radiance data can be downloaded from https://www.eorc.jaxa.jp/ptree/index.html.

747 Code/Data used in this research is available on request from the author.

748 Author contribution. Conceptualization, FFS, AQS and HL; methodology, FFS, AQS

749 and DMX; validation, FFS, AQS and DMX; supervision, HL and JZM; project

750 administration, HL and JZM. All authors discussed the results and contributed to the

751 final version of the paper.

752 Competing interests. The authors declare that they have no conflict of interest.

753 Acknowledgements. This research was primarily supported by the Chinese National

754 Natural Science Foundation of China (G41805016), the Chinese National Key R&D

755 Program of China (2018YFC1506404), the Chinese National Natural Science

756 Foundation of China (G41805070), the Chinese National Key R&D Program of China

757 (2018YFC1506603), the research project of Heavy Rain and Drought-Flood Disasters

758 in Plateau and Basin Key Laboratory of Sichuan Province in China (SZKT201901,

759 SZKT201904), the research project of the Institute of Atmospheric Environment,

760 China Meteorological Administration, Shenyang in China (2020SYIAE07,

761 2020SYIAE02). The numerical calculations in this paper have been done on the

762 supercomputing system in the Supercomputing Center of Nanjing University of

763 Information Science & Technology.

764